symmetry

MDPI

Article

A Microstructural Study of Cu-10Al-7Ag Shape Memory Alloy in As-Cast and Quenched Conditions

Lovro Liverić [1], Wojciech Sitek [2], Przemysław Snopiński [3], Wojciech Maziarz [4] and Tamara Holjevac Grgurić [5,*]

[1] Faculty of Engineering & Centre for Micro- and Nanosciences and Technologies, University of Rijeka, Vukovarska 58, 51 000 Rijeka, Croatia; lovro.liveric@riteh.uniri.hr
[2] Scientific and Didactic Laboratory of Nanotechnology and Material Technologies, Faculty of Mechanical Engineering, Silesian University of Technology, 44-100 Gliwice, Poland; wojciech.sitek@polsl.pl
[3] Department of Engineering Materials and Biomaterials, Faculty of Mechanical Engineering, Silesian University of Technology, 44-100 Gliwice, Poland; przemyslaw.snopinski@polsl.pl
[4] Institute of Metallurgy and Materials Science, Polish Academy of Sciences, 25 Reymont Str., 30-059 Krakow, Poland; maziarz.w@imim.pl
[5] School of Medicine, Catholic University of Croatia, Ilica 242, 10 000 Zagreb, Croatia
* Correspondence: tamara.grguric@unicath.hr

Abstract: Shape memory alloys (SMAs) represent an exceptional class of smart materials as they are able to recover their shape after mechanical deformation, making them suitable for use in actuators, sensors and smart devices. These unique properties are due to the thermoelastic martensitic transformation that can occur during both thermal and mechanical deformation. Cu-based SMAs, especially those incorporating Al and Ag, are attracting much attention due to their facile production and cost-effectiveness. Among them, Cu-Al-Ag SMAs stand out due to their notably high temperature range for martensitic transformation. In this study, a Cu-based SMA with a new ternary composition of Cu-10Al-7Ag wt.% was prepared by arc melting and the samples cut from this casting alloy were quenched in water. Subsequently, the phase composition and the development of the microstructure were investigated. In addition, the morphology of the martensite was studied using advanced techniques such as electron backscatter diffraction (EBSD) and transmission electron microscopy (TEM). The analyzes confirmed the presence of martensitic structures in both samples; mainly 18R ($\beta_{1'}$) martensite was present but a small volume fraction of ($\gamma_{1'}$) martensite also was noticed in the as-quenched sample. The observation of fine, twinned martensite plates in the SMA alloy with symmetrically occurring basal plane traces between the twin variants underlines the inherent correlation between microstructural symmetry and the properties of the material and provides valuable insights into its behavior. The hardness of the quenched sample was found to be lower than the as-cast counterpart, which can be linked to the solutioning of Ag particles during the heat treatment.

Keywords: shape memory alloys; Cu-Al-Ag alloys; heat treatment; microstructure; phase transformations; martensitic transformations

check for updates

Citation: Liverić, L.; Sitek, W.; Snopiński, P.; Maziarz, W.; Grgurić, T.H. A Microstructural Study of Cu-10Al-7Ag Shape Memory Alloy in As-Cast and Quenched Conditions. *Symmetry* **2024**, *16*, 545. https://doi.org/10.3390/sym16050545

Academic Editor: Vasilis K. Oikonomou

Received: 3 April 2024
Revised: 26 April 2024
Accepted: 29 April 2024
Published: 2 May 2024

Copyright: © 2024 by the authors. Licensee MDPI, Basel, Switzerland. This article is an open access article distributed under the terms and conditions of the Creative Commons Attribution (CC BY) license (https://creativecommons.org/licenses/by/4.0/).

1. Introduction

Cu-based shape memory alloys (SMAs) exhibit remarkable properties, such as super elasticity and shape memory effect, attributed to a diffusionless reversible martensitic transformation [1–3]. Due to their affordability and ease of processing, Cu SMAs are utilized in various fields, including medicine, electronics and aerospace [4–7]. Among these alloys, copper-aluminum-based alloys (Cu-Al) are characterized by their exceptional mechanical properties, excellent electrical and thermal conductivity, and relatively low cost compared to other SMAs, such as Ni-Ti alloys [4,7].

Recently, ternary Cu-Al-Mn SMAs have attracted considerable attention. This increased interest stems from the addition of manganese in binary Cu-Al alloys, which serves

to stabilize the β-phase region and extend it towards lower aluminum concentrations. As a result, the β-phase exhibits increased stability against diffusive decomposition [8–12]. As the alloy cools, the β-phase undergoes transformations with disordered order and progresses from β(A2) to β_2(B2) to β_1($L2_1$) [12–16]. These transformations lead to cubic (b.c.c.) superlattice structures such as the Fe_3Al type (DO_3), the CsCl type (B2) and the Cu_2MnAl type ($L2_1$). At lower temperatures, spinodal decomposition can occur between the DO_3 (Cu_3Al) and $L2_1$ (Cu_2AlMn) phases [16]. The transition from A2 to $L2_1$ cannot be suppressed at high aluminum concentrations, resulting in the $L2_1$ phase, known as Heusler alloy (Cu_2AlMn), undergoing a metastable transformation to 6M martensite. Conversely, at lower aluminum concentrations, typically below 16%at., A2 transforms either into A1 (disordered face-centered cubic structure f.c.c.) or into a 2M structure [10–12]. Depending on the chemical composition, various martensite structures can be observed in Cu-based SMA, including hexagonal 2H and rhombohedral structures 9R, 18R, 6R and 3R [11,12,17–19].

To date, there have been only a few studies on the addition of Ag to binary Cu-Al SMAs and ternary Cu-SMA alloys. The addition of Ag to SMA alloys of the Cu-Al system improves their hardness, corrosion resistance, aging properties and magnetic properties, as stated by Silva et al. [13]. Santos et al. [14] attributes the increased microhardness of ternary alloys with 3%at. Ag to the formation of bainite. Cu-Al-Ag SMAs are characterized by the highest temperature of martensitic transformation, primarily between 200 °C and 600 °C, depending on the Al/Ag ratio, so that they are used for high-temperature applications in certain areas [20,21]. Furthermore, the addition of 4%wt. Ag in Cu-Al alloys affects the phase transformations, can promote the formation of pearlitic phases and can change the stability of this pearlitic phase [22]. The precipitation of Ag in Cu-Al-Ag alloys exhibits a zero-order reaction, indicating constant Ag diffusion rates and an interface-controlled formation of Ag-rich phases [2]. Furthermore, the addition of Ag to Cu-based SMAs significantly improves the martensitic transformation, ductility and operating temperature range compared to conventional Cu-Ni-Ti and Cu-Al-Ni SMAs [13,23]. In the study [24], the influence of silver content on the microstructure, martensitic transformation and shape memory effect of Cu-Al-Ag alloys is investigated. The potential for optimizing stability and improving shape memory performance through thermal cycle training and specific adjustments of the silver content for use at high temperatures is demonstrated. The presence of Ag in the Cu-11%wt. Al alloy has a significant influence on the cooling rate, phase formation and martensitic transformation temperatures, providing insights into the optimization of these alloys for specific applications [25]. In addition, Krishna [26], who investigated Cu-XAl-5Mn-2Ag alloys, found that the concentration of aluminum influences martensite formation and has a direct impact on the shape memory effect. Manasijević [27] proved that Cu-Al-Mn-Ag alloys with a higher manganese content yield complete martensite, while those with a lower manganese content exhibit α-phase precipitation.

This investigation will further contribute to the development of Cu-Al-Ag alloys with improved properties and expand their range of applications in various fields. In the paper, an alloy with the composition Cu-10%wt. Al-7%wt. Ag is produced in an electric arc furnace by melting high-purity metals. Morphological and microstructural changes in the alloys were investigated in both the as-cast and quenched states by optical (OM), scanning electron microscopy (SEM) and transmission electron microscopy (TEM). The influence of heat treatment on the microstructure of the investigated alloy was examined using the SEM and TEM-EDS and SEM-EBSD methods. Phase identification was carried out using X-ray diffraction (XRD) and high-resolution X-ray diffraction (XRD), and the hardness of the alloy was determined using the micro-Vickers hardness test.

2. Materials and Methods

The Cu-10Al-7Ag SMA alloy was prepared by melting raw metals (Mateck Material-Technologie & Kristalle, Jülich, Germany): copper (99.9%), aluminum (99.5%), and silver (99.99%). The metals were melted in an electric-arc furnace that had been previously vacuumed and subjected to multiple cycles of argon pumping. The samples underwent

more than four remelting processes for better homogenization and were cast in cylindrical molds with dimensions of 8 × 12 mm. After casting, the samples were quenched in chamber furnaces (OVER, Zagreb, Croatia) at 900 °C for 30 min and rapidly cooled in water.

For metallographic analysis, the samples were prepared by cutting, cold mounting, and grinding with 320#, 600#, 800#, 1200#, and 2400# SiC abrasives. Subsequently, they were polished with 1 µm and ≤0.2 µm diamond paste using Citopress-20 and Tegramin-30 (Struers, Willich, Germany). The prepared samples were etched with a solution of 2.5 g $FeCl_3$, 48 mL CH_3OH, and 10 mL H_2O.

The microstructures were analyzed using an Axio Vert A1 optical microscope (Carl Zeiss NTS GmbH, Oberkochen, Germany), a FEG QUANTA 250 scanning electron microscope (Thermo Fisher, formerly FEI, Waltham, MA, USA) equipped with an energy dispersive X-ray spectroscopy detector (EDS) (Oxford Instruments, Abingdon, UK), and two transmission electron microscopes, Tecnai G2 F20 (200 kV) (TEM) with an energy dispersive X-ray microanalyzer (EDX), a HAADF detector for the scanning transmission technique (STEM), a field emission gun (FEG) and high-resolution Gatan UltraScan and wide-angle SIS Megaview cameras (Thermo Fisher, formerly FEI, USA) and Titan 80–300, FEI S/TEM microscope equipped with spherical aberration correctors in both the probe and imaging optics. The microscope was operated at 300 kV (Thermo Fisher, formerly FEI, USA). The TEM instruments provided SAED, bright and dark field TEM, and HAADF images of a lamellar sample (approximately 10 × 8 µm) prepared by the focused ion beam (FIB) method using the Helios 650HP SEM/FIB dual beam microscope (Thermo Fisher, formerly FEI, USA) with Octane Pro EDS detector (EDAX Inc., Mahwah, NJ, USA).

Electron backscatter diffraction (EBSD) analyses were conducted using a Supra 35 scanning electron microscope (SEM) from Carl Zeiss NTS GmbH, Oberkochen, Germany. The SEM operated at an acceleration voltage of 15 kV, a working distance of 17 mm, a tilt angle of 70°, and utilized step sizes ranging from 0.4 to 0.06 µm. Samples for EBSD analysis were prepared following standard metallographic techniques, involving mechanical grinding with SiC papers, polishing with diamond pastes, and a final polishing step for 1 h using 0.04 µm colloidal silica.

X-ray diffraction (XRD) analysis was performed using a Bruker D8 Advance diffractometer (Bruker Corporation, Billerica, MA, USA) with CuKα radiation. The scans were collected in the 2θ range of 20–90°, with a 2θ step size of 0.02° and a counting time of 0.6 s, under the accelerating voltage of 40 kV and current of 25 mA.

The crystal structure and overall texture of samples in both cast and quenched states were analyzed through high-energy X-ray diffraction measurements at DESY in Hamburg, Germany, utilizing the P07B beamline (87.1 keV, λ = 0.0142342 nm). For phase analysis, diffraction patterns were recorded in continuous mode using a 2D Mar345 Image Plate detector. To ensure textureless measurements, all samples underwent a 180° rotation about the ω-axis during X-ray exposure. To maintain the Bragg condition for satellite reflections, samples were continuously rotated around the ω sample axis by ω < ±10°, with a beam size of 1 × 1 mm^2. Subsequently, the 2D patterns were integrated using the Fit2D software (https://www.esrf.fr/computing/scientific/FIT2D/index.html) and presented in a graph of relative intensity vs. 2Theta angle.

The microhardness of the alloys was determined using the FM-ARS-9000 fully automatic microhardness measurement system (Future-Tech, Kawasaki-City, Japan). A load of HV 100 g and a dwell time of 15 s were applied during the measurements. Prior to microhardness testing, each sample underwent meticulous preparation, involving thorough cleaning, grinding, and polishing to ensure result accuracy. The Vickers microhardness values were calculated as the average of five individual measurements taken from each sample.

3. Results

3.1. Microstructure of the Cu-10Al-7Ag SMA Alloy

Figure 1 shows the optical micrographs (OM) of the Cu-10Al-7Ag SMA alloy in the as-cast state. From the observation of the microstructure, it is clear that the alloy has the

potential to exhibit shape memory properties. As can be seen in Figure 1a, the as-cast sample microstructure consists of coarse grains with a measured average initial size of ~460 µm. The higher magnification OM in Figure 1b documents the presence of martensite needles and indicates the existence of secondary phases (bright precipitates) randomly distributed in the alloy matrix. The precipitation of these secondary phases at room temperature may have occurred due to their limited solubility in the parent matrix. It is worth noting that these precipitate phases could potentially have a detrimental effect on the shape memory properties of the alloy.

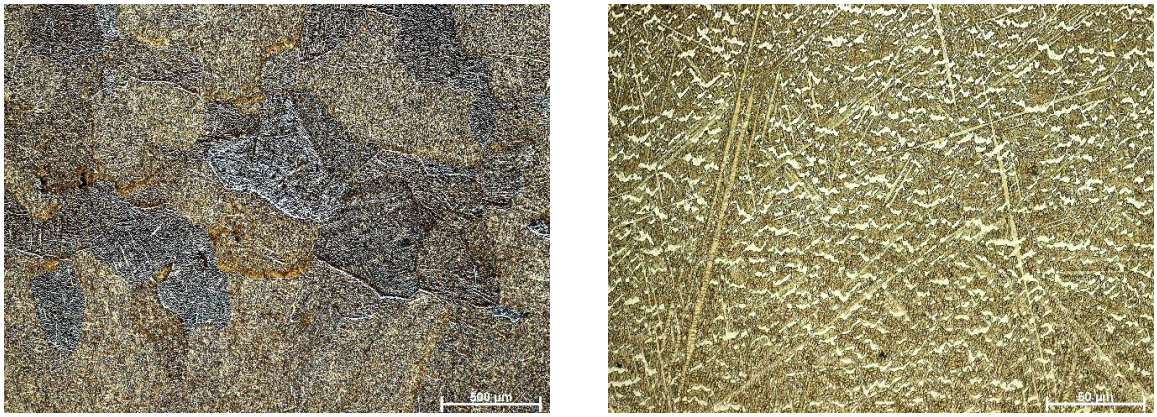

(**a**) (**b**)

Figure 1. Microstructure of the Cu-10Al-7Ag SMA alloy in the as-cast condition: (**a**) low-magnification polarized light OM image, (**b**) high-magnification bright field OM image.

Figure 2 shows the effect of the heat treatment on the microstructure of the Cu-10Al-7Ag SMA alloy. The high cooling rate led to an increased dislocation density [28], which provided numerous heterogeneous nucleation sites for martensite formation with a zigzag and arrow morphology (Figure 2a). A similar martensite variant was also observed by other researchers in the following studies [29]. The higher magnification image also shows the more uniform distribution of silver precipitates within the martensitic matrix, Figure 2b. In addition, it can be seen that the size of the grains decreased to ~400 µm after quenching. The finer grains of SMA can help to reduce the brittleness and improve the shape memory properties of the samples [30].

(**a**) (**b**)

Figure 2. Microstructure of the Cu-10Al-7Ag SMA alloy in the quenched condition: (**a**) low-magnification polarized light OM image, (**b**) high-magnification bright field OM image.

The microstructures and phase compositions were then examined using SEM/EDX. The SEM images of as-cast and quenched Cu-10Al-7Ag are shown in Figure 3, while the

corresponding EDX results are listed in Tables 1 and 2, respectively. It is worth noting that both images were taken at the same magnification to emphasize the microstructural differences between the two states.

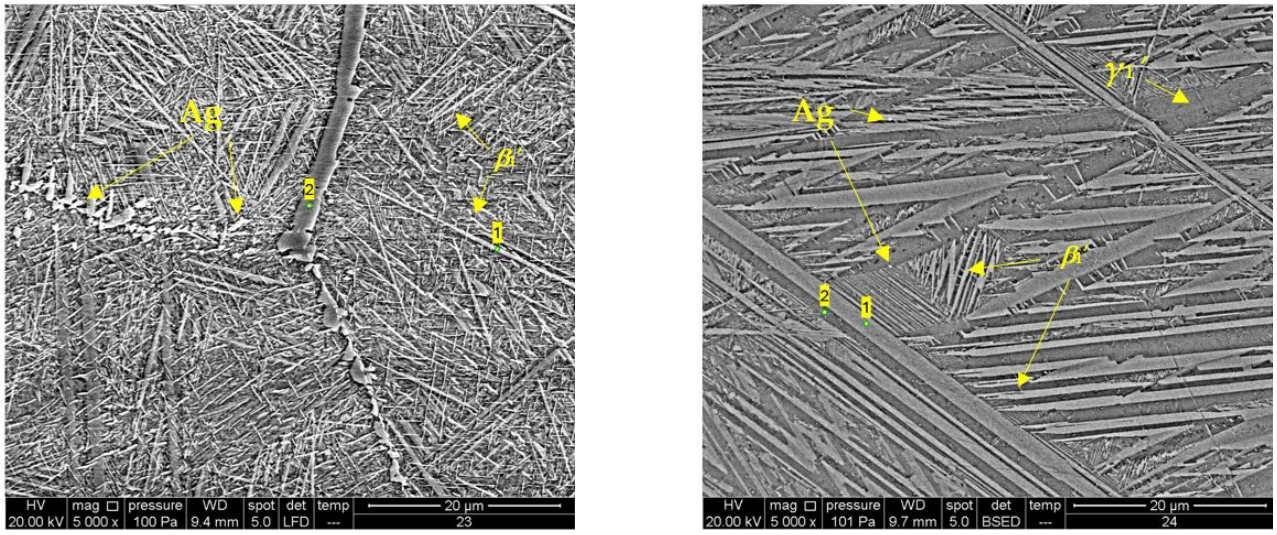

(**a**) (**b**)

Figure 3. SEM microstructures of the Cu-10Al-7Ag SMA alloy (**a**) as-cast condition, (**b**) quenched.

Table 1. Results of EDS chemical composition microanalysis of as-cast sample.

	Al	Cu	Ag
Point 1	9.21 ± 0.20	80.87 ± 0.55	6.78 ± 0.24
Point 2	10.28 ± 0.42	81.51 ± 0.63	8.21 ± 0.52

Table 2. Results of EDS chemical composition microanalysis of quenched sample.

	Al	Cu	Ag
Point 1	9.70 ± 1.11	80.41 ± 1.70	9.89 ± 1.42
Point 2	10.30 ± 0.90	81.2 ± 1.10	8.50 ± 1.05

As shown in Figure 3a, the microstructure of the as-cast sample consists of V-type $\beta_{1'}$-martensite and several fine precipitates. The EDX results in Table 1 show that the precipitates in the grain interior are enriched in Cu and Al, while the precipitates in the form of an almost continuous layer along a grain boundary region are enriched with silver.

After quenching, the precipitates, which form a continuous layer along the grain boundary, have disappeared. In this state, the Ag precipitates are uniformly distributed in the matrix of Cu-10Al-7Ag alloy, as shown in Figure 3b. It is worth noting that quenching resulted in the formation of coarse martensite plates, which may indicate the presence of another type of martensite, possibly the $\gamma_1{}'$, 2H type. In addition, the Cu-10Al-7Ag alloy was found to exhibit predominantly the self-accommodating zig-zag morphology typical of 18R martensite in the quenched state. The martensitic transformation observed in the Cu-10Al-7Ag SMA alloy illustrates the fundamental role of symmetry in determining the shape memory properties of the alloy. The transition from the highly symmetric β-phase to the martensitic phases with lower symmetry (e.g., 18R, 2H) underlines how closely symmetry changes are linked to the functional behavior of the alloy.

Both conventional and high-energy X-ray diffraction techniques were used to further analyze the phase composition. The conventional X-ray diffractogram is shown in Figure 4a. Phase identification revealed the presence of $\beta_1{}'$-martensite and silver phases in both samples.

It is noteworthy that in the quenched sample, the peaks of the β_1'-martensite phase almost disappear at higher 2theta angles. This phenomenon could be due either to a reduction in the content of the β_1'-martensite phase after quenching or to changes in the macrotexture. However, it is also evident that the peaks corresponding to the β_1'-martensite phase are more pronounced in the quenched state around the 2theta angle of 45 degrees. Moreover, the peaks associated with the Ag phase in the as-cast state are clearly recognizable as precipitates that are unevenly distributed at the grain border, but disappear after quenching, which is consistent with the observations of the microstructure in SEM and as a secondary phase on Figure 1b in OM.

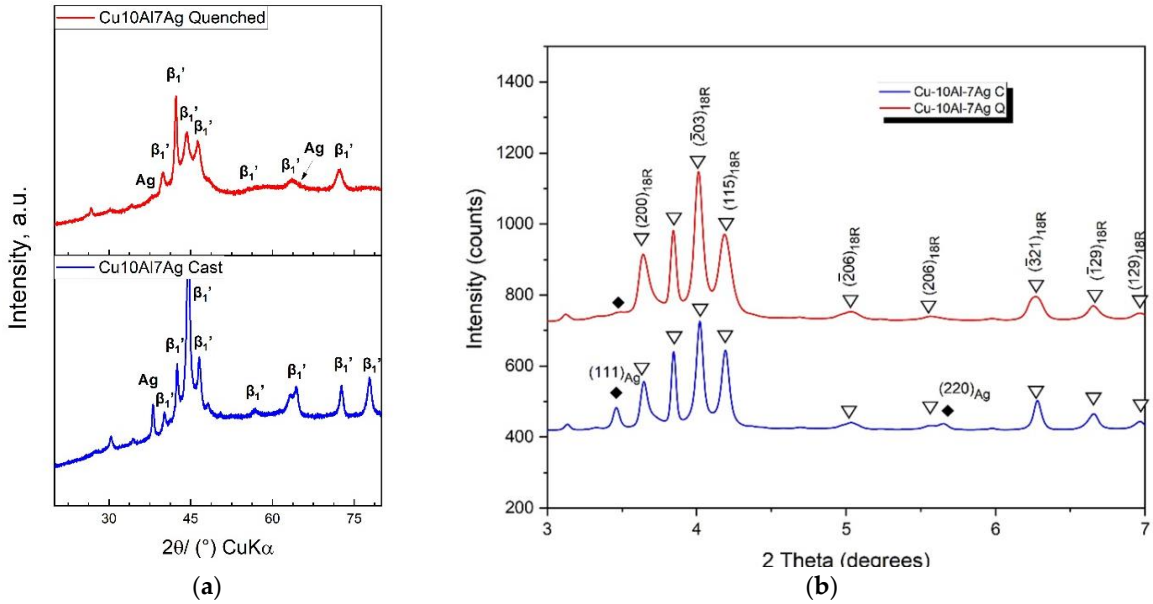

Figure 4. XRD diffractogram of Cu-10Al-7Ag SMA alloy: (**a**) regular XRD diffractogram, (**b**) high-energy X-ray diffraction measurements from synchrotron.

To gain insight into the grain structure, an EBSD analysis was performed. Figure 5a shows the IPF map, which includes the low-angle grain boundaries (red), the high-angle grain boundaries (green) and the twin boundaries (black). The colors in the IPF Z-map correspond to the Z-direction within the reference frame of the sample, as shown in Figure 5b. General observation EBSD analysis revealed differences from the microstructural observations in the SEM, particularly in the identification of twin boundaries and the presence of small round particles. These differences may be due to the different capabilities of the two techniques, with SEM Figure 3 revealing variations in composition and EBSD Figure 5 providing data on crystallographic orientation.

Figure 5a confirms that the martensite phase has a distinct zigzag morphology, which is consistent with the optical microscopy results. The color represents different martensite orientations. The grain boundary distribution histogram shows that high-angle grain boundaries predominate and account for about 80% of the grain boundary fraction (HAGBs + twin boundaries). It is also worth noting that a large proportion of the HAGBs are twin boundaries, which is reflected in an increased proportion of boundaries with a misorientation angle of 60 degrees. These boundaries are clearly visible in the IPF-Z EBSD map as they mainly separate the parallel β_1'-martensite plates. Significantly, twin boundaries are present in both straight, parallel shapes and curved configurations, indicating the coexistence of both coherent and incoherent twin boundaries within the microstructure. The high proportion of these boundaries indicates a well-defined microstructural mechanism that underpins the alloy's excellent shape memory and pseudoelastic properties. According to the grain size distribution histograms in Figure 6, the microstructure in Figure 6b consists of martensite plates with a dominant size of about 1 µm.

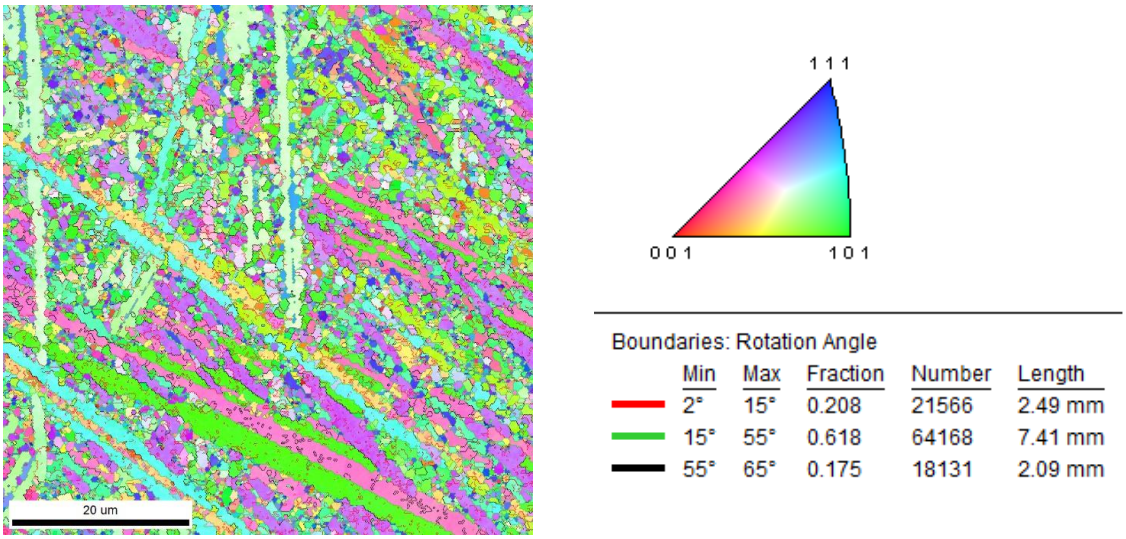

(**a**) (**b**)

Figure 5. Results of the EBSD investigation of cast sample: (**a**) IPF-Z image, (**b**) IPF map reference frame and the statistical information about boundary fraction.

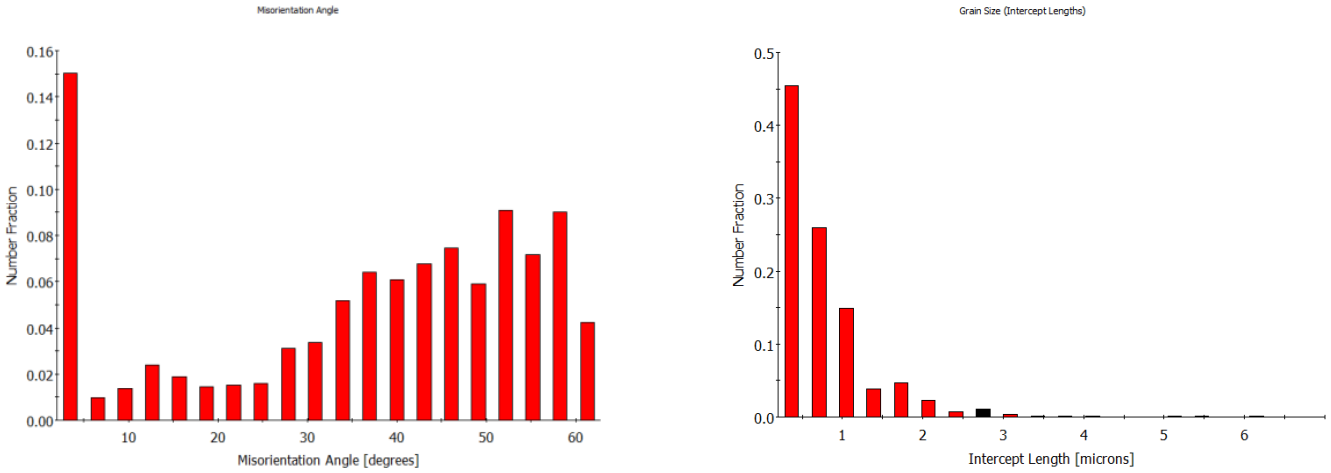

(**a**) (**b**)

Figure 6. Results of the EBSD investigation of cast sample: (**a**) histogram of grain boundary misorientation distribution, (**b**) histogram of grain size distribution.

Further insight into the dislocation properties was gained by plotting the Kernel Average Misorientation Map. It is known that the KAM value directly reflects the geometrically necessary dislocation density, i.e., the higher the KAM value, the higher the GND density. Figure 7 shows that there is no large accumulation of dislocations in the as-cast state. The highest KAM values are seen in the large martensite plates, indicating a higher GND accumulation in this area, which is probably due to the presence of dense networks of misfit dislocations inside plates. The average KAM value measured is 0.60°.

Figure 8 shows the IPF-Z map of the quenched sample. It is noticeable that the microstructure appears much finer in the quenched state than in the as-cast state. Figure 9 shows the histograms of the EBSD investigation of the grain boundary misorientation and the grain size distribution of the quenched sample. Most of the grains have a size of less than 1 µm, Figure 9b. Analysis of the grain boundary distribution histogram shows a notable shift where low angle grain boundaries (LAGBs) now dominate and account for approximately 51% of the total, Figure 9a. This increase in the proportion of LAGBs can be

attributed to dislocation multiplication that occurs during heat treatment [31]. Of particular interest is the observation that the fraction of twin boundaries increased to about 21% after quenching, as indicated by the histogram of the boundary distribution, which shows a peak around a misorientation angle of 60 degrees, Figure 9. This suggests that the fraction of the twinned 18R phase is increased after quenching. Such mechanisms favor the increase in the proportion of LAGBs because they reduce the total energy of the system by organizing the dislocations in more stable configurations. The presence of more LAGBs usually indicates a material that can better resist plastic deformation, which is particularly important for applications that require high elasticity under mechanical stress.

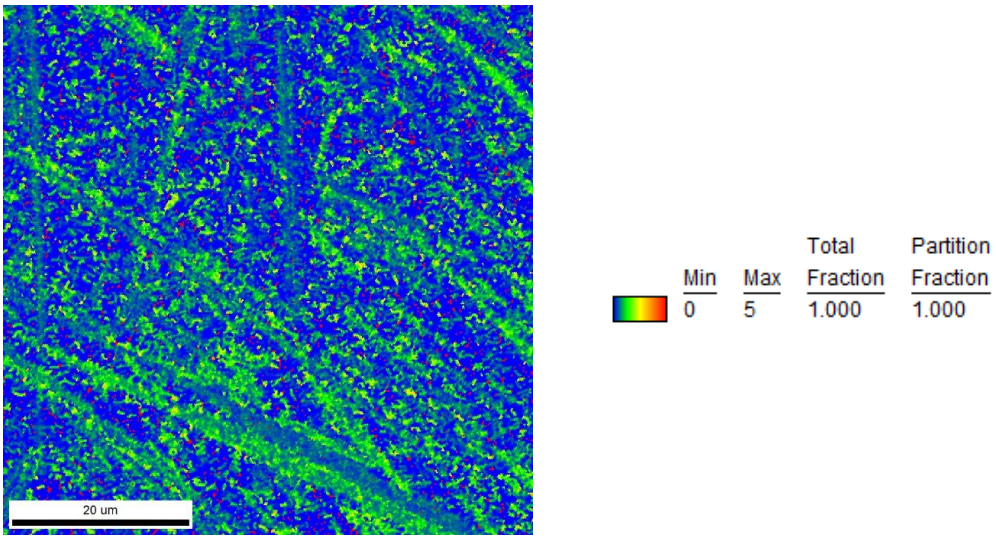

(**a**) (**b**)

Figure 7. Kernel Average Misorientation map of Cu-10Al-7Ag SMA cast sample (**a**) and corresponding legend showing color coding in KAM map (**b**).

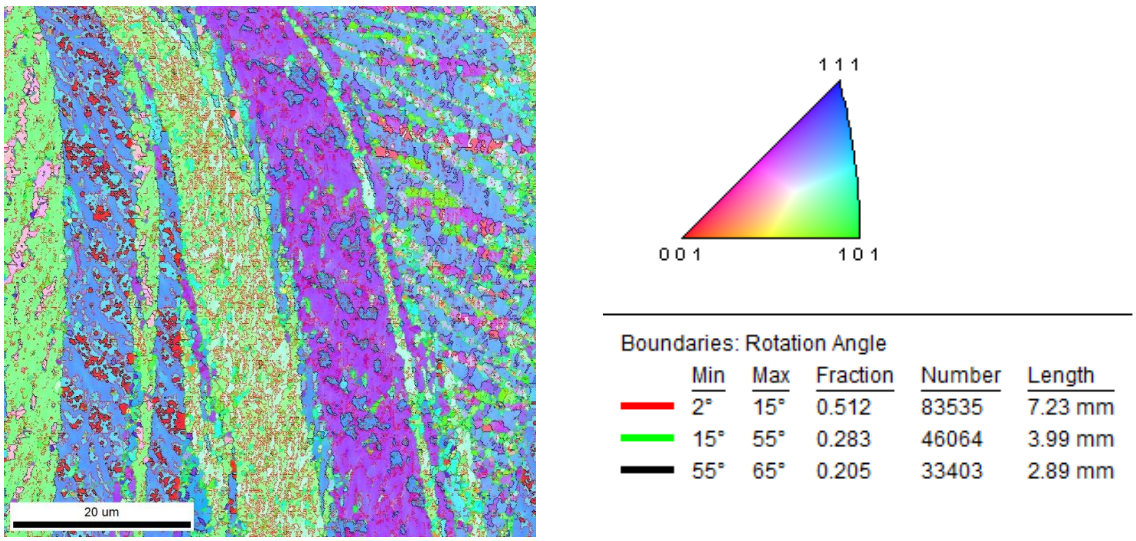

(**a**) (**b**)

Figure 8. Results of the EBSD investigation of Cu-10Al-7Ag SMA quenched sample: (**a**) IPF-Z image, (**b**) IPF map reference frame and the statistical information about boundary fraction.

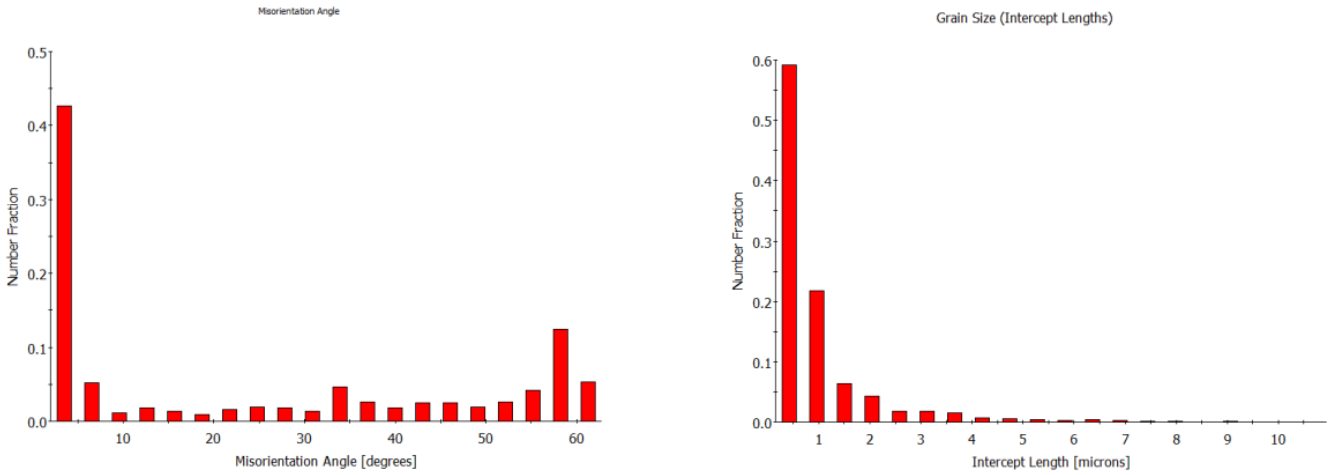

(**a**) (**b**)

Figure 9. Results of the EBSD investigation of Cu-10Al-7Ag SMA quenched sample: (**a**) histogram of grain boundary misorientation distribution, (**b**) histogram of grain size distribution.

Figure 10 shows the KAM map of the Cu-10Al-7Ag SMA alloy sample in its quenched state. It can be seen that the increased KAM values are mainly concentrated around the Low Angle Grain Boundaries (LAGBs) and reach higher average values for the quenched sample (0.91°) than for the as-cast sample (0.60°). This increase in the KAM value is obviously due to the increased presence of geometrically necessary dislocations. According to the work of Yi et al. [32], the thermal cycle involving the martensitic transformation must coincide with the occurrence of dislocations at the interface. In addition, the phase transformation leads to the formation of subgrain boundaries, which contributes to the propagation of dislocations. Consequently, a significantly higher number of generated dislocations can be assumed in the quenched sample compared to its as-cast counterpart, which is consistent with the electron backscatter diffraction (EBSD) data.

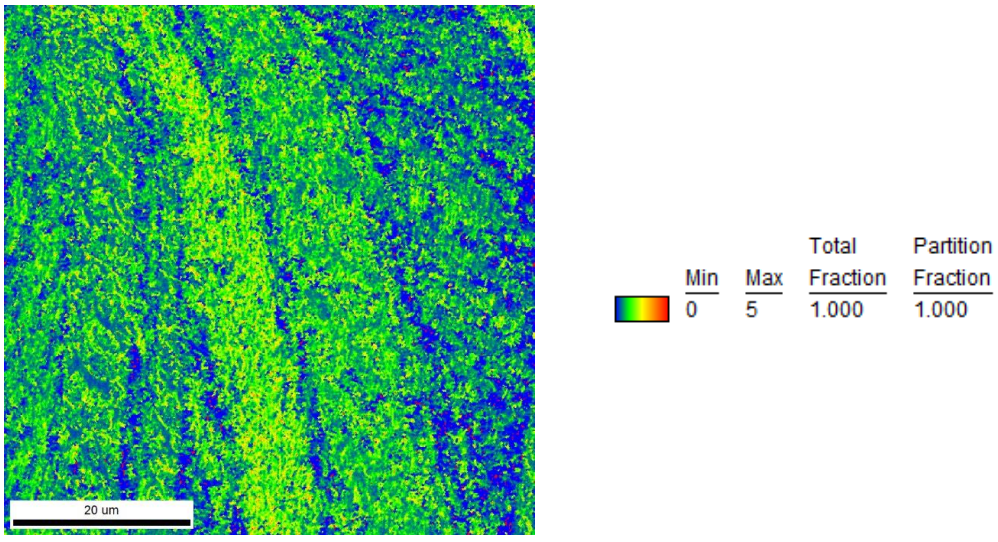

(**a**) (**b**)

Figure 10. Kernel Average Misorientation map of Cu-10Al-7Ag SMA quenched sample (**a**) and corresponding legend showing a color coding in KAM map (**b**).

STEM observations were carried out to show the distribution of the most important alloying elements. Figure 11 shows the STEM-HAADF image together with the correspond-

ing elemental distribution maps. As can be observed, the elemental maps show a random (homogeneous) distribution of Ag precipitates in the as-cast matrix of the sample. These precipitates have a length of about 0.5 to several microns. This image also shows that the alloy matrix is rich in Cu and Al.

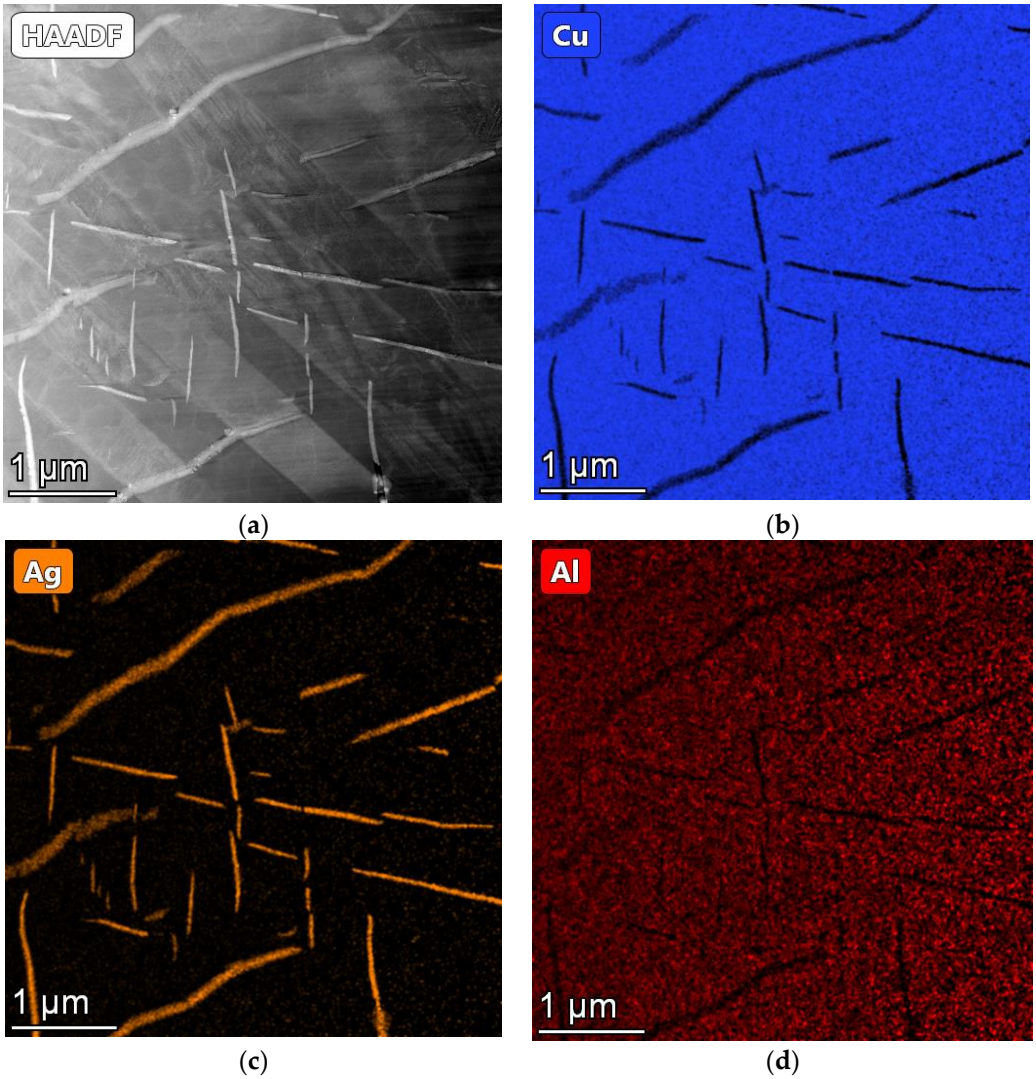

Figure 11. STEM HAADF and EDS elemental maps of the Cu-10Al-7Ag SMA alloy in as-cast condition (**a**) STEM-HAADF image, (**b**) Cu element distribution map, (**c**) Ag element distribution map, (**d**) Al element distribution map.

Examination of the microstructural changes using SEM and EBSD techniques sheds light on the symmetrical characteristics inherent in martensitic transformations. The patterns of twin boundaries and the transformation-induced changes in the microstructure highlight the fundamental symmetry principles that govern these phase transitions in the alloys.

Figure 12 shows the results of the quantitative chemical analysis performed for the indicated areas, showing the composition of the three microstructural constituents observed in the as-cast sample. It can be seen that the general composition of the as-cast sample (matrix plus Ag precipitates) differs slightly from the nominal composition. The measured composition is depleted in both Al and Ag, which is most likely due to high heterogeneity of the as-cast sample. This heterogeneity can be mainly related to the different density of Ag precipitates in the microstructure, as they also contain a considerable amount of Cu and a small amount of Al, as can be seen in Figure 12.

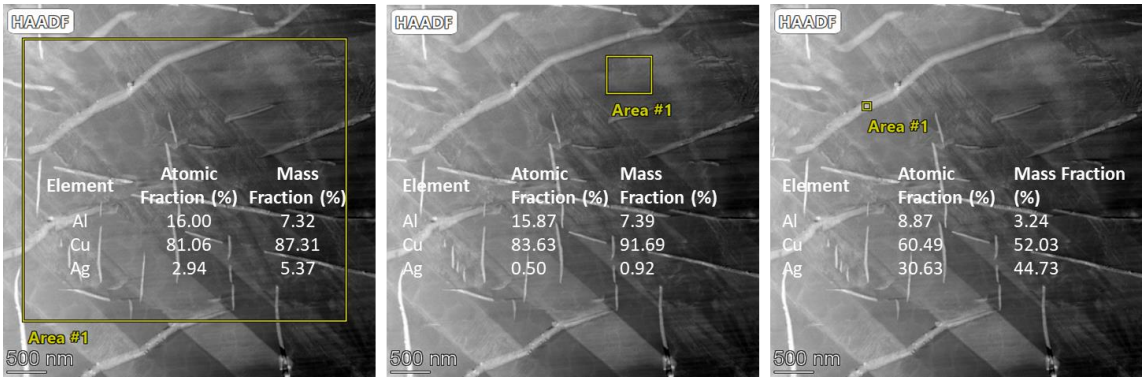

Figure 12. STEM HAADF and results of chemical analyses performed in the indicated areas of the Cu-10Al-7Ag SMA alloy in as-cast condition.

Figure 13 shows the bright field (BF), dark field (DF) and corresponding selected area diffraction pattern (SADP) of specimen in the as-cast condition. It reveals the clearly contrasting martensite plates having a width of 150–800 nm which were identified as 18R phase. SADP vell fits to the [010] zone axis of the R18 martensite with very low monoclinic distortion of $\beta = 88.7°$. This pattern exhibits a contrast with a 0.619 nm periodicity typical of the 18R stacking sequence that is visible in the DF image taken from the (0012) spot. The streaks between stacking spots could be attributed to the presence of many structural faults inside the martensite variants, probably produced by the internal stresses.

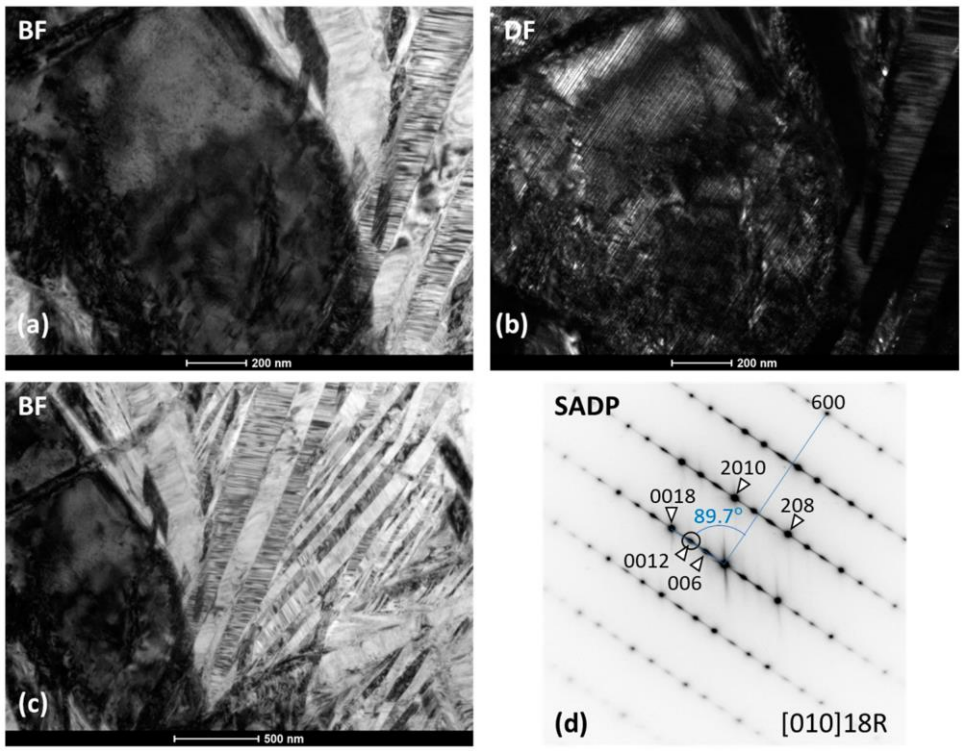

Figure 13. TEM images of the Cu-10Al-7Ag SMA alloy in cast condition: (**a**) bright-field TEM image taken at higher magnification and (**b**) dark field TEM image revealing 18R stacking sequence, (**c**) bright field TEM image taken at low magnification and corresponding (**d**) dark-selected area diffraction pattern (SADP).

To gain greater insight into the complex microstructure of the SMA alloy, observations in the scanning transmission mode (STEM) were performed. The BF-STEM image, Figure 14a, confirms that the alloy has a martensitic structure, with fine, twinned martensite

plates present throughout. In Figure 14a, the angles between the traces of the basal planes in the twin variants and the twin boundary were measured to be 57°, which indicates that the basal plane traces appear symmetrically in the twin variants. In addition, the corresponding STEM-HAADF (Z-contrast) image in Figure 14b reveals minor chemical composition fluctuations within the martensite plates. However, it should be mentioned here that this change in contrast may be related to the different orientation of the martensite plates.

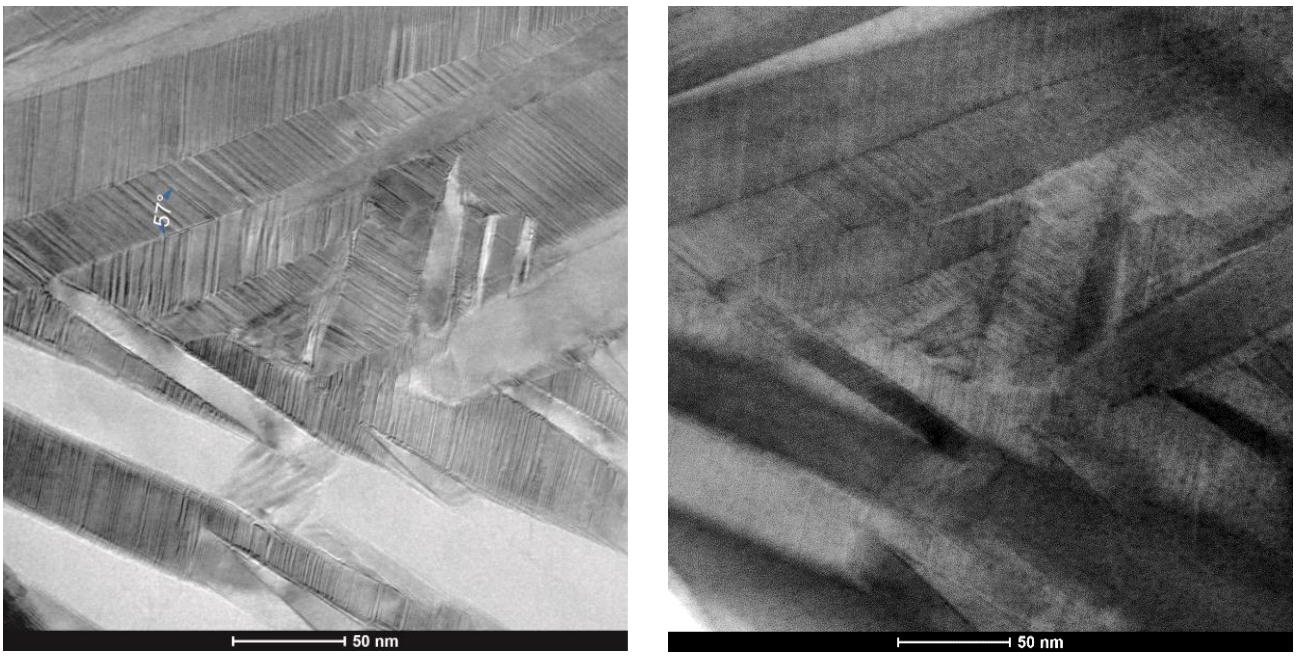

(**a**) (**b**)

Figure 14. STEM (**a**) and HAADF (**b**) images showing the martensite matrix morphology in Cu-10Al-7Ag SMA alloy in cast condition.

Further observations were made on the quenched sample. Figure 15 shows the STEM-HAADF image with the corresponding element maps. Figure 15a reveals significant evolution of the microstructure after quenching. It can be clearly seen that the precipitates of the Ag phase have a different size and morphology. Figure 15b shows Ag nanoprecipitates with the mean size of about 10 nm, and more evenly distributed due to the rapid cooling rate restricting their growth and resulting in a finer dispersion. A similar microstructure was recently described by Silva et al. [33] for a Cu-11%Al-10%Mn-3%Ag alloy. In addition, there are some undissolved Ag phase clusters in the microstructure, indicating that complete dissolution was not achieved after quenching.

These morphological differences between the as-cast and quenched states have a significant impact on the mechanical and functional properties of the alloy, as smaller, more uniformly distributed precipitates affect the mechanical properties and alter the thermomechanical properties by more effectively retaining dislocations and distributing stress more evenly across the matrix.

Figure 16a–d is a set of TEM images of the as-quenched sample showing BF image and corresponding DF images and SAED pattern. The TEM observations confirm the presence of the β_1'-martensite phase. Two types of martensite plates can distinguish with thickness range from 100 to 500 nm and few nanometers, respectively (fine plates marked by ovals in the DF images). Such configuration of the martensite plates is due to the self-accommodation character of the martensitic microstructure formed during thermoelastic martensitic transformation. The electron diffraction pattern registered from two variants of martensite plates being in twin orientation was indexed as 18R structure with the [010] zone axis, Figure 16c. Dark field images (DF-1 and DF-2) are taken from (0018) spots of two

variants being in a twin relationship. However, apart from the main spots taken for the DF image, additional small spots also must be considered (indicated by the arrows) for the formation of the DF image responsible for the fine martensite plates visible in DF images.

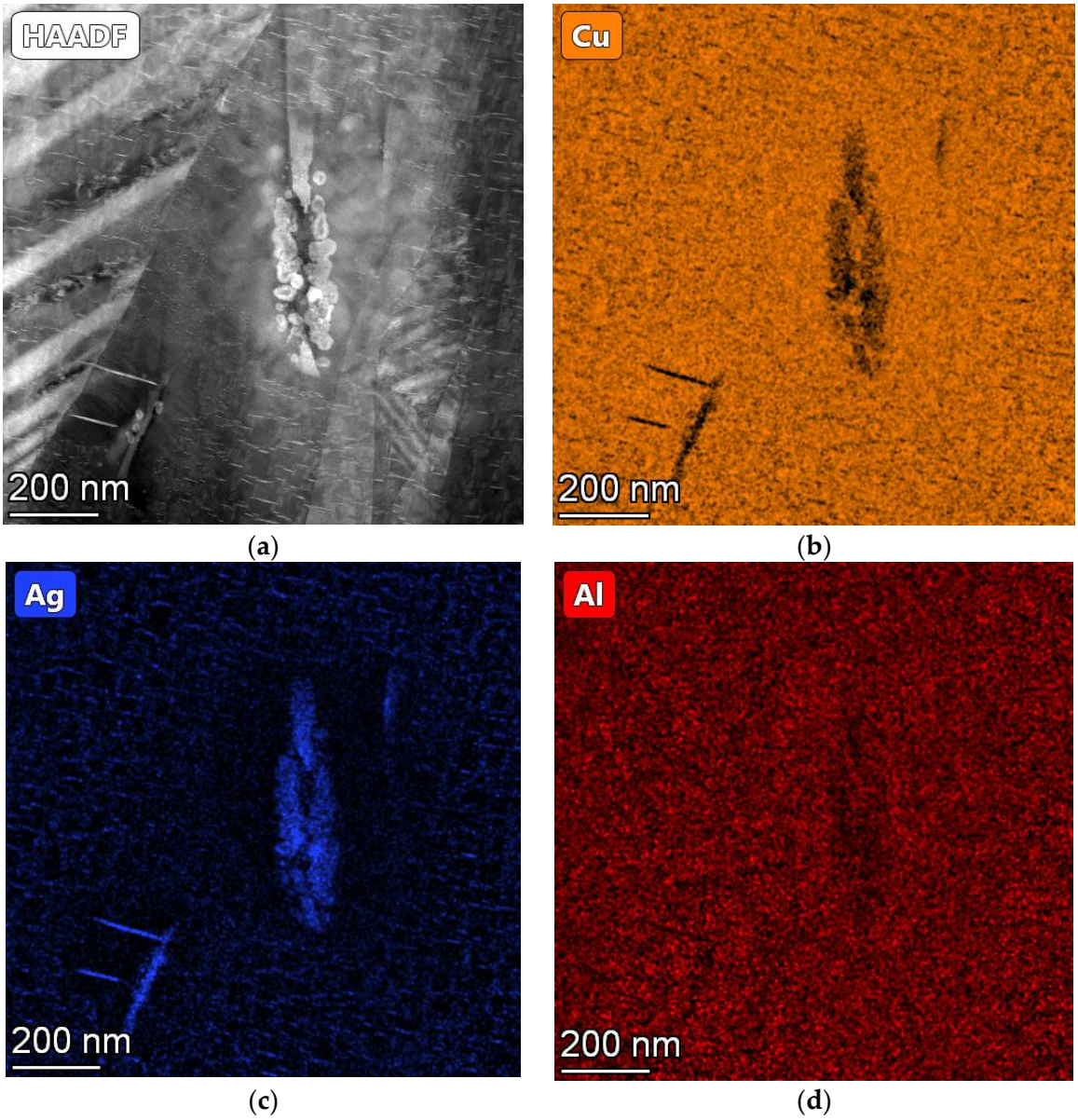

Figure 15. STEM HAADF and EDS maps of the Cu-10Al-7Ag SMA alloy in quenched condition. (**a**) STEM-HAADF image, (**b**) Cu element distribution map, (**c**) Ag element distribution map, (**d**) Al element distribution map.

The TEM images provided above reveal a predominance of the β' phase. However, upon careful analysis of the TEM lamellae, a small volume fraction amount of thermally induced 2H-martensitic Al_4Cu_9 ($\gamma_{1'}$) phase, with a plate-like morphology was observed (see Figure 17) in the quenched sample. It is worth noting that this observation is consistent with the results of the SEM analysis but was not confirmed by X-ray diffraction.

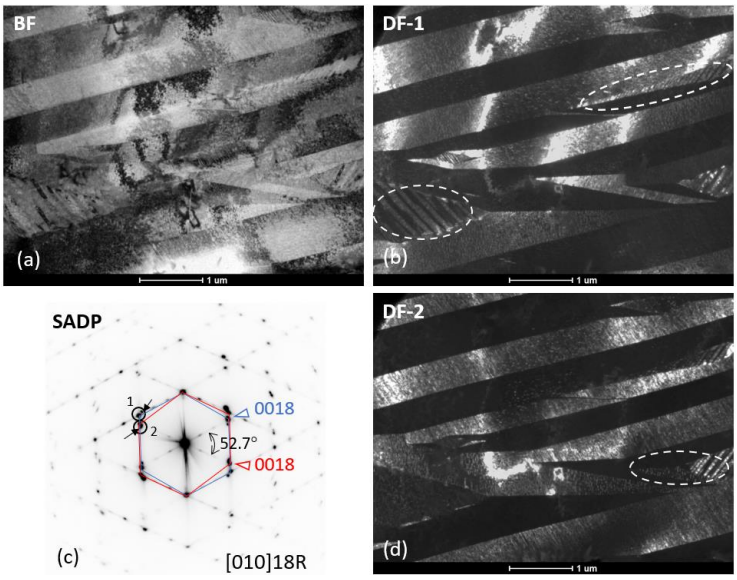

Figure 16. TEM images of the Cu-10Al-7Ag SMA alloy in quenched condition: (**a**) bright-field TEM image, (**b**,**d**) dark-field TEM images and (**c**) selected area diffraction pattern (SADP).

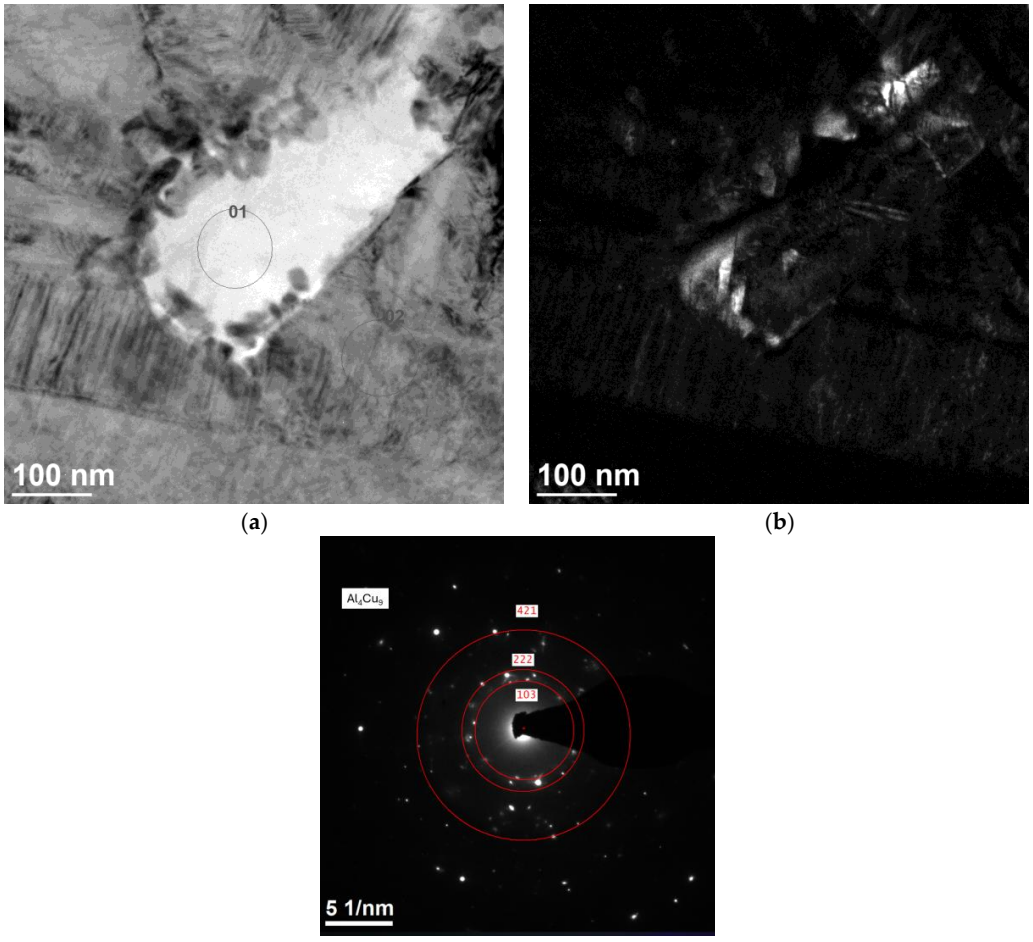

Figure 17. TEM images of the Cu-10Al-7Ag SMA alloy in quenched condition: (**a**) bright-field TEM image, (**b**) dark-field TEM image, and (**c**) selected area diffraction pattern (SADP) obtained from the 01-circle area shown in (**a**) indicating the presence of Al_4Cu_9 ($\gamma_{1'}$) phase. Note that around the Al_4Cu_9 ($\gamma_{1'}$), the $\beta_{1'}$ martensite plates are visible.

According to the literature, the martensitic transformation in Cu-Al alloys occurs during rapid quenching. By cooling at high cooling rates, β phase changes into β_1 parent austenite phase of $L2_1$ (a type of DO_3 superlattice) [34]. The $D0_3$ ordered parent β austenitic phase transforms then into modulated 2H or 18R martensite, or a combination of both, depending on various factors such as alloy composition, temperature, applied stress magnitude, and crystal orientation [35].

According to the study of Sedlák et al., within a certain range of aluminum and manganese content, both $\beta_{1'}$ and $\gamma_1{}'$ martensite phases coexist, which is in line with the findings presented in our article. The $\gamma_1{}'$ phase remains stable even upon heating back up to room temperature due to thermal hysteresis [36].

3.2. Effect of Quenching on the Alloy Hardness

The Cu-10Al-7Ag alloy in the as-cast state exhibits higher microhardness values compared to the quenched state (Table 3). This is typical behavior for Cu-SMA materials and is consistent with previous studies of SMAs. [11–14,37–41]

Table 3. Microhardness of Cu-Al-Ag SMA alloy.

Hardness	**HV**					
Cu-10Al-7Ag Alloy	**1**	**2**	**3**	**4**	**5**	**Average**
As-cast state	225.68	287.79	323.21	278.72	323.34	278.85
Quenched state	186.57	250.05	184.20	222.53	181.80	210.84

The slight variance in the hardness between the tested values, in both as-cast and quenched conditions can be ascribed to the formation of mechanically induced martensite in stressed areas, occurring under high indentation loads [42].

Studies have shown that the introduction of Ag particles into binary Cu-Al alloys increases their microhardness by influencing the nucleation rate and the activation energy of the eutectoid decomposition reaction [23,43].

The Ag additions improve the microhardness of Cu-Al alloys by hindering dislocation movement, refining the grain structure and influencing the phase behavior.

Nevertheless, the Ag particles are located within the Cu/Al metal matrix. Therefore, in this study, the presence of Ag particles, although it contributes to the strengthening of the matrix, is considered marginal compared to other sources of hardening, such as grain size, or does not change the microhardness values [13,23].

4. Conclusions

In this article, the microstructure of the Cu-10Al-7Ag SMA alloy in as-cast and quenched conditions was investigated throughout. The following conclusions can be drawn from this study:

In the Cu-10Al-7Ag SMA alloy, stable martensite formed even in the as-cast state without additional heat treatment, which indicates its potential for exhibiting shape memory properties.

The hardness of the quenched sample was found to be lower than the as-cast counterpart, which can be linked to the solutioning of Ag particles during the heat treatment.

Using the SEM, SEM-EBSD, XRD and TEM techniques, the presence of type 18R martensite was confirmed in both the as-cast and quenched samples, while the small volume fraction presence of type 2H martensite was noticed using the TEM technique in quenched sample.

Understanding the role of alloy composition, especially with the addition of Ag, in martensitic transformation is crucial for designing SMAs with tailored properties. While the presence of the martensite phase is necessary for the shape memory effect, it alone does not guarantee this behavior. Our findings reveal that not all SMAs in the martensite phase exhibit the shape memory effect, highlighting the critical role of additional factors such as

composition, microstructure, and thermal history in influencing shape memory behavior. Further investigations could explore the influence of other alloying elements and optimize heat treatment processes to enhance the performance of Cu-Al-Ag alloys.

This research contributes to the broader field of SMAs, shedding light on the interplay between the material state, microstructure, and phase composition. The findings provide valuable insights for engineering applications where shape memory behavior is desired.

Author Contributions: Conceptualization, L.L. and T.H.G.; methodology, L.L., P.S. and T.H.G.; validation, L.L., W.S., P.S., W.M. and T.H.G.; formal analysis, L.L., P.S., W.M. and T.H.G.; investigation, L.L., W.S., P.S., W.M. and T.H.G.; resources, L.L., W.S., P.S. and W.M.; writing—original draft preparation, L.L. and P.S.; writing—review and editing, L.L., W.S., P.S., W.M. and T.H.G.; visualization, L.L., P.S. and T.H.G.; supervision, W.S., W.M. and T.H.G. All authors have read and agreed to the published version of the manuscript.

Funding: This work has been supported in part by University of Rijeka under the project: uniri-iskusni-tehnic-23-293.

Data Availability Statement: Data will be made available upon request.

Conflicts of Interest: The authors declare no conflicts of interest.

References

1. Mazzer, E.M.; da Silva, M.R.; Gargarella, P. Revisiting Cu-Based Shape Memory Alloys: Recent Developments and New Perspectives. *J. Mater. Res.* **2022**, *37*, 162–182. [CrossRef]
2. Silva, R.A.G.; Adorno Ii, A.T.; Carvalho Ii, T.M.; Ii, A.G.M.; Ii, C.M.A.S. Precipitation Reaction in Alpha-Cu-Al-Ag Alloys. *Rev. Matéria V* **2011**, *16*, 747–753. [CrossRef]
3. Grgurić, T.H.; Manasijević, D.; Kožuh, S.; Ivanić, I.; Anžel, I.; Kosec, B.; Bizjak, M.; Bajsić, E.G.; Balanović, L.; Gojić, M. The Effect of the Processing Parameters on the Martensitic Transformation of Cu-Al-Mn Shape Memory Alloy. *J. Alloys Compd.* **2018**, *765*, 664–676. [CrossRef]
4. Alaneme, K.K.; Okotete, E.A. Reconciling Viability and Cost-Effective Shape Memory Alloy Options—A Review of Copper and Iron Based Shape Memory Metallic Systems. *Eng. Sci. Technol. Int. J.* **2016**, *19*, 1582–1592. [CrossRef]
5. Ren, C.X.; Wang, Q.; Hou, J.P.; Zhang, Z.J.; Yang, H.J.; Zhang, Z.F. Exploring the Strength and Ductility Improvement of Cu–Al Alloys. *Mater. Sci. Eng. A* **2020**, *786*, 139441. [CrossRef]
6. Najah, S.; Al-Humairi, S. Cu-Based Shape Memory Alloys: Modified Structures and Their Related Properties. In *Recent Advancements in the Metallurgical Engineering and Electrodeposition*; Springer: Berlin/Heidelberg, Germany, 2020.
7. Dobrzański, L.A.; Dobrzański, L.B.; Dobrzańska-Danikiewicz, A.D.; Dobrzańska, J. Nitinol Type Alloys General Characteristics and Applications in Endodontics. *Processes* **2022**, *10*, 101. [CrossRef]
8. Silva, R.A.G.; Paganotti, A.; Adorno, A.T.; Santos, C.M.A.; Carvalho, T.M. Characteristics of the Cu-18.84 at.%Al-10.28 at.%Mn-1.57 at.%Ag Alloy after Slow Cooling from High Temperatures. *J. Therm. Anal. Calorim.* **2015**, *121*, 1233–1238. [CrossRef]
9. Mallik, U.S.; Sampath, V. Effect of Alloying on Microstructure and Shape Memory Characteristics of Cu–Al–Mn Shape Memory Alloys. *Mater. Sci. Eng. A* **2008**, *481–482*, 680–683. [CrossRef]
10. Santos, C.M.A.; Adorno, A.T.; Oda, N.Y.; Sales, B.O.; Silva, L.S.; Silva, R.A.G. Phase Transformations and Aging of the Cu72.9Al15.0Mn10.5Ag1.6 Alloy. *J. Alloys Compd.* **2016**, *685*, 587–592. [CrossRef]
11. Liverić, L.; Holjevac Grgurić, T.; Mandić, V.; Chulist, R. Influence of Manganese Content on Martensitic Transformation of Cu-Al-Mn-Ag Alloy. *Materials* **2023**, *16*, 5782. [CrossRef]
12. Liverić, L.; Grgurić, T.H.; Bajsić, E.G.; Kršulja, M. Effect of Silver Addition on Cu-Based Shape Memory Alloys. *Chem. Biochem. Eng. Q.* **2023**, *37*, 153–161. [CrossRef]
13. Silva, R.A.G.; Paganotti, A.; Gama, S.; Adorno, A.T.; Carvalho, T.M.; Santos, C.M.A. Investigation of Thermal, Mechanical and Magnetic Behaviors of the Cu-11%Al Alloy with Ag and Mn Additions. *Mater. Charact.* **2013**, *75*, 194–199. [CrossRef]
14. Santos, C.M.A.; Adorno, A.T.; Paganotti, A.; Silva, C.C.S.; Oliveira, A.B.; Silva, R.A.G. Phase Stability in the Cu-9 Wt%Al-10 Wt%Mn-3 Wt%Ag Alloy. *J. Phys. Chem. Solids* **2017**, *104*, 145–151. [CrossRef]
15. Pilz, C.B.; Matsumura, E.L.; Paganotti, A.; Cornejo, D.R.; Silva, R.A.G. Microstructure and Phase Stability of CuAlMnAgZr Multicomponent Alloys. *Mater. Chem. Phys.* **2020**, *241*, 122343. [CrossRef]
16. Velazquez, D.; Romero, R. Spinodal Decomposition and Martensitic Transformation in Cu–Al–Mn Shape Memory Alloy. *J. Therm. Anal. Calorim.* **2017**, *130*, 2007–2013. [CrossRef]
17. Zárubová, N.; Novák, V. Phase Stability of CuAlMn Shape Memory Alloys. *Mater. Sci. Eng. A* **2004**, *378*, 216–221. [CrossRef]
18. Qian, S.; Geng, Y.; Wang, Y.; Pillsbury, T.E.; Hada, Y.; Yamaguchi, Y.; Fujimoto, K.; Hwang, Y.; Radermacher, R.; Cui, J.; et al. Elastocaloric Effect in CuAlZn and CuAlMn Shape Memory Alloys under Compression. *Philos. Trans. R. Soc. A Math. Phys. Eng. Sci.* **2016**, *374*, 20150309. [CrossRef] [PubMed]

19. Suru, M.G.; Lohan, N.M.; Pricop, B.; Mihalache, E.; Mocanu, M.; Bujoreanu, L.G. Precipitation Effects on the Martensitic Transformation in a Cu-Al-Ni Shape Memory Alloy. *J. Mater. Eng. Perform.* **2016**, *25*, 1562–1569. [CrossRef]
20. Fernández, J.; Isalgue, A.; Franch, R. Effect of Thermal Cycling on CuAlAg Shape Memory Alloys. *Mater. Today Proc.* **2015**, *2*, S805–S808. [CrossRef]
21. Ferreira, R.O.; Silva, L.S.; Silva, R.A.G. Thermal Behavior of As-Annealed CuAlMnAgZr Alloys. *J. Therm. Anal. Calorim.* **2021**, *146*, 595–600. [CrossRef]
22. Adorno, A.T.; Benedetti, A.V.; Da Silva, R.A.G.; Blanco, M. Influence of the Al Content on the Phase Transformations in Cu-Al-Ag Alloys. *Eclet. Quim.* **2003**, *28*, 33–38. [CrossRef]
23. Seifollahzadeh, P.; Alizadeh, M.; Szabó, Á.; Gubicza, J.; El-Tahawy, M. Microstructure and Mechanical Behavior of Cu–Al–Ag Shape Memory Alloys Processed by Accumulative Roll Bonding and Subsequent Annealing. *Crystals* **2022**, *12*, 1167. [CrossRef]
24. Guilemany, J.M.; Fernandez, J.; Zhang, X.M. TEM Study on the Microstructure of Cu-Al-Ag Shape Memory Alloys. *Mater. Sci. Eng. A* **2006**, *438–440*, 726–729. [CrossRef]
25. Silva, R.A.G.; MacHado, E.S.; Adorno, A.T.; Magdalena, A.G.; Carvalho, T.M. Completeness of B-Phase Decomposition Reaction in Cu-Al-Ag Alloys. *J. Therm. Anal. Calorim.* **2012**, *109*, 927–931. [CrossRef]
26. Krishna, T.S.V.; Rao, D.S. Effect of Aluminium on Microstructure and Shape Memory Effect in Cu-Al-Ag-Mn Shape Memory Alloys. *Aust. J. Mech. Eng.* **2022**, 1–17. [CrossRef]
27. Manasijevićmanasijević, D.; Holjevac, T.; Grgurić, G.; Balanovićbalanović, L.; Stamenković, U.S.; Gorgievski, M.; Gojićgojić, M. Effect of Mn Content on the Microstructure and Phase Transformation Temperatures of the Cu-Al-Mn-Ag Shape Memory Alloys. *Chem. Biochem. Eng. Q.* **2020**, *58*, 293–299. [CrossRef]
28. Izadinia, M.; Dehghani, K. Structure and Properties of Nanostructured Cu-13.2Al-5.1Ni Shape Memory Alloy Produced by Melt Spinning. *Trans. Nonferrous Met. Soc. China* **2011**, *21*, 2037–2043. [CrossRef]
29. Gurau, G.; Gurau, C.; Fernandes, F.M.B.; Silva, R.J.C.; Marin, F. Using High Speed High Pressure Torsion for Cu–13Al–4Ni Shape Memory Alloy Processing. *Trans. Indian Inst. Met.* **2021**, *74*, 2459–2469. [CrossRef]
30. Shafeeq, M.M.; Gupta, G.K.; Malik, M.M.; Sampath, V.; Modi, O.P. Influence of Quenching Methods on Martensitic Transformation and Mechanical Properties of P/M Processed Cu–Al–Ni–Ti Shape Memory Alloys. *Powder Metall.* **2016**, *59*, 271–280. [CrossRef]
31. Yi, J.; Wan, L.; Shu, T.; Zhang, X.; Liu, F.; Cheng, G.J. Unleashing Multi-Scale Mechanical Enhancement in NiTi Shape Memory Alloy via Annular Intra-Laser Deposition with Homogenized Ti2Ni Nanoprecipitates. *Acta Mater* **2024**, *262*, 119418. [CrossRef]
32. Suresh, K.S.; Bhaumik, S.K.; Suwas, S. Effect of Thermal and Thermo-Mechanical Cycling on the Microstructure of Ni-Rich NiTi Shape Memory Alloys. *Mater. Lett.* **2013**, *99*, 150–153. [CrossRef]
33. Silva, R.A.G.; Paganotti, A.; Jabase, L.; Adorno, A.T.; Carvalho, T.M.; Santos, C.M.A. Ag-Rich Precipitates Formation in the Cu–11%Al–10%Mn–3%Ag Alloy. *J. Alloys Compd.* **2014**, *615*, S160–S162. [CrossRef]
34. Canbay, C.A.; Karaduman, O.; Ünlü, N.; Baiz, S.A.; Özkul, İ. Heat Treatment and Quenching Media Effects on the Thermodynamical, Thermoelastical and Structural Characteristics of a New Cu-Based Quaternary Shape Memory Alloy. *Compos. B Eng.* **2019**, *174*, 106940. [CrossRef]
35. Ge, Y.; Vronka, M.; Veřtát, P.; Karlik, M.; Hannula, S.P.; Heczko, O. Deformation Twinning with Different Twin-Boundary Mobility in 2H Martensite in Cu–Ni–Al Shape Memory Alloy. *Acta Mater.* **2022**, *226*, 117598. [CrossRef]
36. Sedlák, P.; Seiner, H.; Landa, M.; Novák, V.; Šittner, P.; Mañosa, L. Elastic Constants of Bcc Austenite and 2H Orthorhombic Martensite in CuAlNi Shape Memory Alloy. *Acta Mater.* **2005**, *53*, 3643–3661. [CrossRef]
37. Kožuh, S.; Gojić, M.; Ivanić, I.; Holjevac Grgurić, T.; Kosec, B.; Anžel, I. The Effect of Heat Treatment on the Microstructure and Mechanical Properties of Cu-Al-Mn Shape Memory Alloy. *Kem. U Ind.* **2018**, *67*, 11–17. [CrossRef]
38. Jain, A.K.; Hussain, S.; Kumar, P.; Pandey, A.; Dasgupta, R. Effect of Varying Al/Mn Ratio on Phase Transformation in Cu–Al–Mn Shape Memory Alloys. *Trans. Indian Inst. Met.* **2016**, *69*, 1289–1295. [CrossRef]
39. Silva, R.A.G.; Gama, S.; Paganotti, A.; Adorno, A.T.; Carvalho, T.M.; Santos, C.M.A. Effect of Ag Addition on Phase Transitions of the Cu-22.26 at.%Al-9.93 at.%Mn Alloy. *Thermochim. Acta* **2013**, *554*, 71–75. [CrossRef]
40. Gholami-Kermanshahi, M.; Wu, Y.Y.; Lange, G.; Chang, S.H. Effect of Alloying Elements (Nb, Ag) on the Damping Performance of Cu–Al–Mn Shape Memory Alloys. *J. Alloys Compd.* **2023**, *930*, 167438. [CrossRef]
41. Taha, A.S.; Hammad, F.H. Application of the Hall-Petch Relation to Microhardness Measurements on Al, Cu, Al-MD 105, and Al-Cu Alloys. *Phys. Status Solidi A* **1990**, *119*, 455–462. [CrossRef]
42. Ćorić -Mladen Franz, D. Properties of Thermally Treated CuZn27Al3 Shape Memory Alloy. *Stroj. Vestn. J. Mech. Eng.* **2009**, *55*, 623–632.
43. Adorno, A.T.; Silva, R.A.G. Isothermal Decomposition Kinetics in the Cu–9%Al–4%Ag Alloy. *J. Alloys Compd.* **2004**, *375*, 128–133. [CrossRef]

Disclaimer/Publisher's Note: The statements, opinions and data contained in all publications are solely those of the individual author(s) and contributor(s) and not of MDPI and/or the editor(s). MDPI and/or the editor(s) disclaim responsibility for any injury to people or property resulting from any ideas, methods, instructions or products referred to in the content.